Hindawi
Structural Control and Health Monitoring
Volume 2023, Article ID 1465042, 21 pages
https://doi.org/10.1155/2023/1465042

Research Article

Seismic Optimization for Hysteretic Damping-Tuned Mass Damper (HD-TMD) Subjected to White-Noise Excitation

Yue Xiang,[1,2] Ping Tan ,[1,2] Hui He,[3] and Qianmin Chen[1,2]

[1]*School of Civil Engineering, Guangzhou University, Guangzhou, China*
[2]*Key Laboratory of Earthquake Resistance, Earthquake Mitigation and Structural Safety, Ministry of Education, Guangzhou University, Guangzhou, China*
[3]*Hunan Institute of Technology, Hengyang 421002, China*

Correspondence should be addressed to Ping Tan; ptan@gzhu.edu.cn

Received 10 October 2022; Revised 20 January 2023; Accepted 28 January 2023; Published 23 February 2023

Academic Editor: Yoshiki Ikeda

The hysteretic damping tuned mass damper (HD-TMD) is composed of a spring element, a hysteretic damping (HD) element, and a mass. The HD force is proportional to the displacement of the tuned mass damper (TMD). Recently, the application of HD-TMD has emerged, but its optimal design is still lacking. To fill this academic gap, numerical solutions for optimal parameters of HD-TMD subjected to white-noise excitation were obtained based on the H_2 optimization criterion. Performance balance optimization with a weighting factor was carried out to improve the response of a structure with the HD-TMD system. A set of earthquake records and harmonic excitations were conducted to prove the effectiveness of the optimal numerical solutions and the performance balance design. It was found that the performance of the HD-TMD is slightly better than that of the traditional optimized TMD. As a real TMD application of HD-TMD, the variable friction pendulum TMD (VFP-TMD) was selected to experience earthquakes with the proposed optimal methods. Results showed that the optimal solutions provided the best performance but raised the problem of difficulty in maintaining linearity with a large displacement. Nevertheless, the performance balance design helped reduce this defect and provided impressive seismic mitigation capacity. Compared with the optimal numerical solution results, the performance balance design demonstrated 2.847% of loss in the maximum structural displacement reduction rate and 3.709% of loss in the root mean square reduction rate during the earthquake-excited period, respectively.

1. Introduction

Structural control has been studied and applied in many engineering fields [1–3], such as mechanical, civil, and aerospace, to mitigate structural response against external loads. In civil engineering, the tuned mass damper (TMD) is well recognized as one of the most efficient and reliable passive control strategies. First-born TMD is known as the dynamic vibration absorber which was initially intended to suppress the vibration of watercraft during sailing [4]. Instead of the series connection of the spring and damping element, Ormondroyd and Den Hartog [5] improved the above elements into parallel settings which broaden the bandwidth of the frequency response function (FRF). To provide the optimal parameters with different circumstances, several typical closed-form solutions of traditional viscous TMD were summarized and derived by Warburton [6].

As one of the classic optimization, Crandall and Mark [7] proposed the H_2 optimization theory to minimize the vibration energy of the system in the frequency domain. In this optimal criterion, the area under the frequency response curve of the system is minimized. Optimal solutions based on H_2 optimization for TMD of the undamped and damped structures were derived by Asami et al. [8, 9]. Bakre and Jangid [10] developed the optimal parameter solution through numerical optimization and curve-fitting techniques based on H_2 optimization theory for damped structures. Analytical studies of TMD with nonlinear viscous damping subjected to white-noise excitation were conducted

by Chung et al. [11]. Tigli [12] derived the H_2 optimal parameter solutions targeting the optimization of velocity and pointed out that the velocity criterion provides the best overall performance with the least complexity in the design equations. As the extension application of H_2 optimization, a three-element TMD was proposed and the closed-form solutions were derived [13]. The optimal parameter formulas of a nonlinear tuned viscous mass damper (TVMD) under white noise were derived by Chen and Tan [14]. Closed-form solutions for TVMD acceleration control under white-noise seismic excitation of the undamped structure were obtained and proven to be effective in the mitigation of lightly damped structures [15].

Instead of the high cost, high maintenance, and short servicing time for viscous dampers of traditional TMD, HD-TMD presents stable mitigation capacity for various excitation amplitudes with the benefits of easy-replacement and low cost. From the perspective of the differential equations of motion, the damping force of the HD-TMD is related to the variate of differential equations of motion, which had resulted in the widened effective control bandwidth and the increased of robustness. Hysteretic damping (HD) was proposed to describe the mechanism of materials [16], in which the damping force is proportional to the displacement of the mass and is in phase with its velocity [17–19]. Modified hysteretic models were proposed by Muravskii [20] to investigate the frequency-independent characteristics of a single degree of freedom (SDOF) system. Later, Liu [21] provided Reid's hysteretic oscillators with friction force dependence on displacement to state the HD mechanism. Nevertheless, previous works of HD were mainly focused on theoretical study. Recently, Kang et al. [22] and Matta et al. [23–25] proposed Reid-TMD and homogeneous tangential friction bidirectional TMD (HT-BTMD) to realize the physical form of HD-TMD device. Rate-independent damping mechanism was studied by Nagarajaiah et al. [26] to further reveal the mitigation capacity of TMD-NSD [27]. Furthermore, the experiments [24] and numerical analysis [28] were conducted to illustrate the effectiveness of the HD-TMD by HT-BTMD. However, the optimal seismic designs of HD-TMD subjected to white-noise excitation are still lacking.

In reality, the movement conditions of TMD have limited in a certain range of space thanks to the limitation of the installation site of TMD, the requirement of space utilization rate, and the actual mechanical deformation limit requirements. The optimal design procedure and experiments for TMD were proposed and conducted to reduce structural dynamic responses with the limitation of its stroke [29–31]. The fragility was found to be significantly influenced by the TMD stroke and structural acceleration [32]. A lifecycle cost optimization considering the correct quantification of the costs and stroke of TMD was provided for profitable investment [33]. Furthermore, the meaning of controlling the stroke of TMD can be widespread to the other important academic fields of structure control, for example, for the interstory isolated system to control the simplified upper structure. Therefore, it is necessary to construct a performance balance design for the HD-TMD that achieves the destination of providing the desired dual-target control performance by the actual needs.

To bridge the mentioned gaps, in this study, the optimal design and control performance of HD-TMD subjected to white-noise excitation were investigated. In the derivation of the optimal solutions of the HD-TMD, the H_2 optimization criterion was applied, and the performance of the optimal solutions was successfully assessed. To improve the performance of the structure with the HD-TMD system, the performance balance optimization was proposed with a weighting factor that depends on the tolerance ratio. Finally, verifications were taken to examine the effectiveness of the proposed optimization methods with the specific available HD-TMD device.

2. Analysis Model for Structure with HD-TMD

It should be noted that the HD-TMD represents a type of practical TMDs, whose absolute value of the damping force is linear with the stiffness force as shown in the following equation:

$$F_D = \operatorname{sign}(\dot{x}_t)\eta k_t |x_t|, \tag{1}$$

where sign() represents the signum function; x_t denotes the relative displacement of TMD; η denotes the HD ratio; and k_t means the stiffness of the TMD. The signum function reveals that the HD-TMD damping force is perpendicular to the stiffness force in the complex field.

The hysteretic damping loop of HD-TMD is illustrated in Figure 1. As shown in Figure 1, the absolute value of the damping force increases proportionally with the relative displacement of the TMD. The HD-TMD can be described as a displacement-dependent TMD that can be achieved by altering the friction damping output, where the range of applications for the model of HD-TMD can be simply found with the damping behavior that is caused by the variable friction settings. For example, Reid-TMD [22], variable friction pendulum tuned mass damper (VFP-TMD) [23, 28], and HT-BTMD [24, 25]. The former stresses the stiffness force from the spring into the friction plate by the design of the device, whereas the latter two change the friction coefficient on the sphere of movement and assume the normal force of friction to be constant. Above-mentioned TMDs obey the Coulomb friction theory. The HD-TMD is a symbolic model that summarized the property of hysteretic damping characteristic and represents these devices precisely, symbolically, and simply. It should be noted that the realistic range to apply the proposed HD-TMD model remains expanded, not limited by the thoughts discussed, and is expected to reveal more.

TMD control theories are mostly applied to the first mode of the structure, which affects the structural response the most under earthquake excitations. An SDOF structure with an HD-TMD system is presented in Figure 2. Note that all the bodies were assumed to remain in the elastic range. m_1, k_1, and c_1 denote the mass, stiffness, and damping of the structure, respectively, and m_t is the mass of the HD-TMD. In addition, $\ddot{x}_g$ stands for ground acceleration. Using the

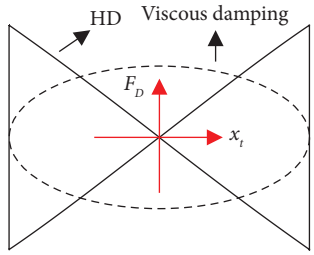

Figure 1: Hysteretic damping loop for HD and viscous damping.

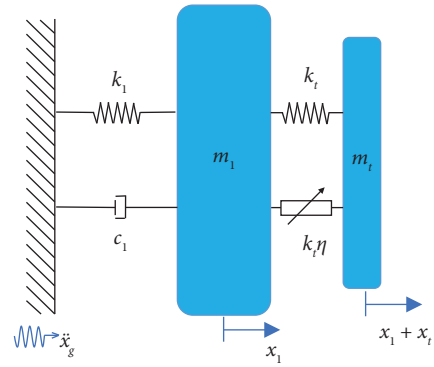

Figure 2: Structure with the HD-TMD system.

Lagrangian method, the equations of motion for the structure with the HD-TMD system can be expressed as follows:

$$\begin{cases} (m_1 + m_t)\ddot{x}_1 + m_t\ddot{x}_t + c_1\dot{x}_1 + k_1x_1 = -(m_1 + m_t)\ddot{x}_g, \\ m_t\ddot{x}_1 + m_t\ddot{x}_t + k_tx_t + \text{sign}(\dot{x}_t)\eta|x_t|k_t = -m_t\ddot{x}_g, \end{cases} \tag{2}$$

where x_1 denote the displacement of the structure relative to the ground. Hence, the dimensionless equations of motion were further derived as follows:

$$\begin{cases} (1 + \mu_t)\ddot{x}_1 + \mu_t\ddot{x}_t + 2\xi_1w_1\dot{x}_1 + {w_1}^2x_1 = -(1 + \mu_t)\ddot{x}_g, \\ \ddot{x}_1 + \ddot{x}_t + {w_t}^2x_t + \text{sign}(\dot{x}_t)\eta|x_t|{w_t}^2 = -\ddot{x}_g. \end{cases} \tag{3}$$

To standardize the subsequent treatment, the following nondimensionalized terms were introduced, as listed in Table 1.

Xiang et al. [28] demonstrated that VFP-TMD with HD characteristic owns linear behavior in the frequency domain and earthquake records with different excitation amplitudes. Associated with the experiments that Matta [24] had performed, the HD-TMD exhibited linear behavior in the application of civil engineering. Frequency domain transformation [20, 26] on HD force in equation (3) is conducted as follows. For a harmonic motion in the form $x_t = X_te^{i\omega t}$, where X_t is a positive amplitude of vibrations response in the frequency domain (for $w > 0$)

$$\eta|x_t|{w_t}^2\text{sign}(\dot{x}_t) = \eta|x_t|{w_t}^2\frac{\dot{x}_t}{|\dot{x}_t|} = \eta\left|X_te^{i\omega t}\right|{w_t}^2\frac{i\omega X_te^{i\omega t}}{\left|i\omega X_te^{i\omega t}\right|}. \tag{4}$$

Based on the Euler formula, $|e^{i\omega t}| = 1$. The equation of (4) can be further obtained as follows:

$$\eta|x_t|{w_t}^2\text{sign}(\dot{x}_t) = \eta X_t{w_t}^2\frac{i\omega X_te^{i\omega t}}{\omega X_t} = \eta X_t{w_t}^2ie^{i\omega t}. \tag{5}$$

Hence, the displacement FRFs for structure and HD-TMD were obtained by Laplace transformation in terms of complex quantities as follows:

$$\begin{aligned} H_1(i\lambda) &= \frac{w_1^2X_1}{f_0} = \frac{-\lambda^2 + i\eta f^2(1 + \mu_t) + f^2(1 + \mu_t)}{\lambda^4 - \lambda^2\left(1 + f^2(1 + \mu_t)\right) + f^2 - 2\xi_1f^2\eta\lambda +} \\ &\quad \frac{}{i\left[-2\xi_1\lambda^3 + 2\xi_1f^2\lambda - \eta f^2(1 + \mu_t)\lambda^2 + \eta f^2\right]}, \\ H_t(i\lambda) &= \frac{w_1^2X_t}{f_0} = \frac{2\xi_1\lambda i + 1}{\lambda^4 - \lambda^2\left(1 + f^2(1 + \mu_t)\right) + f^2 - 2\xi_1f^2\eta\lambda +} \\ &\quad \frac{}{i\left[-2\xi_1\lambda^3 + 2\xi_1f^2\lambda - \eta f^2(1 + \mu_t)\lambda^2 + \eta f^2\right]}, \end{aligned} \tag{6}$$

Table 1: Notations.

Notations	Definition
$w_1 = \sqrt{k_1/m_1}$	Frequency of the structure
$w_t = \sqrt{k_t/m_t}$	Frequency of TMD
$\xi_1 = c_1/(2m_1w_1)$	Damping ratio of the structure
$\mu_t = m_t/m_1$	Mass ratio of TMD
$f = w_t/w_1$	Frequency ratio of TMD
$\lambda = w/w_1$	Frequency ratio of excitation

where X_1 represent the frequency response of displacement for structure in the frequency domain.

3. H_2 Optimization for HD-TMD

To minimize the vibration energy of the overall frequencies of the system, one of the classical design methods, H_2 optimization, was widespread for TMD design, in which the excitation was meant to be processed as the white noise with a uniform power spectral density function. Although many other approaches [34–36] address the optimal energy dissipation capability of the tuned mass damper for variable performance indexes (the acceleration response of the structure, the multi-performance design approaches, etc.), the H_2 optimization for the HD-TMD and SDOF structure is more classic, as well as one of the foundations for the evolutional optimization theories. Especially, it is suitable for the primary structure being subjected to random and complex forms of excitations instead of harmonic excitations in the field of stochastic mechanics. In this section, numerical solutions are derived and parametric studies are conducted for the HD-TMD.

3.1. Theoretical Derivation. As a mature vibration control optimization, H_2 criterion is applied by minimizing the mean square displacement of the structure. Thus, the performance index subjected to white-noise excitation is described by [6].

$$\sigma_1{}^2(\mu_t, f, \eta) = S_0 \int_{-\infty}^{\infty} \left|H_1(i\lambda, \mu_t, f, \eta)\right|^2 \mathrm{d}\lambda, \tag{7}$$

where variance equals the mean square displacement of the structure for a random quantity with zero means. S_0 denotes the normalized constant spectral intensity. The performance indexes can be evaluated by integrating the square of FRF. Without losing generality, the inherent damping of the structure was neglected in this study, and the objective of the optimization was to optimize the HD-TMD parameters for the undamped structure. The square calculation on FRF can be obtained as follows:

$$\left|H_1(\xi_1, i\lambda)\right|^2 = \frac{\left[\lambda^2 - f^2(1+\mu)\right]^2 + \left[\eta f^2(1+\mu)\right]^2}{\left[\lambda^4 - \lambda^2\left(1 + f^2(1+\mu)\right) + f^2 - 2\xi_1 f^2 \eta\lambda\right]^2 + \left[-2\xi_1\lambda^3 + 2\xi_1 f^2\lambda + \eta f^2 - \eta f^2(1+\mu)\lambda^2\right]^2}. \tag{8}$$

By introducing $\xi_1 = 0$, the expression can be performed as follows:

$$\left|H_1(i\lambda)\right|^2 = \frac{\lambda^4 - 2B_2\lambda^2 + B_0^2}{\left[\lambda^4 - \lambda^2(A_1 + iA_4) + A_2 + iA_3\right]\left[\lambda^4 - \lambda^2(A_1 - iA_4) + A_2 - iA_3\right]}, \tag{9}$$

where

$$\begin{cases} A_1 = 1 + (1+\mu)f^2, \\ A_2 = f^2, \\ A_3 = \eta f^2, \\ A_4 = \eta f^2(1+\mu), \end{cases} \qquad \begin{cases} B_2 = f^2(1+\mu), \\ B_0 = f^2(1+\mu)\sqrt{\left(1+\eta^2\right)}. \end{cases} \tag{10}$$

To avoid the complexity of solving the integral calculation, the residue theorem is deployed as a common standard treatment of H_2 optimization to simplify the infinite integral. Normally, simplification expressions can be quoted from the literature [7]. It should be aware that despite the change in the excitation conditions and response parameters, the denominators of the FRFs for traditional viscous TMD remain the same, whose real part of it consists of even orders of frequency variable as well as the imagined part of it consists of odd orders of frequency variable [6, 13]. However, for HD-TMD, the denominator of FRFs exhibit different properties at the complex combination terms in the even order and the missing odd terms of the denominator, which fail in applying the simplification expressions [7, 13, 37] in the literature to bypass the infinite integral of the square calculation for the FRF of HD-TMD. To the limited knowledge of the authors, the simplification results for the infinite integral of the FRF of HD-TMD with the residue theory have been not found in the

past. Therefore, it is urgent to derive simplification results for the infinite integral of the FRF of HD-TMD instead of numerical integral calculation.

To apply the residue theorem, the first step is to factorize the denominator of $|H_1(i\lambda)|^2$. The denominator of $|H_1(i\lambda)|^2$ can be decomposed as follows:

$$\begin{aligned}&\left[\lambda^4-\lambda^2(A_1+iA_4)+A_2+iA_3\right]\left[\lambda^4-\lambda^2(A_1-iA_4)+A_2-iA_3\right]\\&=\left[\left(\lambda^2+\lambda_1^2\right)\left(\lambda^2+\lambda_2^2\right)\right]\left[\left(\lambda^2+\lambda_3^2\right)\left(\lambda^2+\lambda_4^2\right)\right],\\&=\left[(\lambda-i\lambda_1)(\lambda+i\lambda_1)(\lambda-i\lambda_2)(\lambda+i\lambda_2)\right]\left[(\lambda-i\lambda_3)(\lambda+i\lambda_3)(\lambda-i\lambda_4)(\lambda+i\lambda_4)\right],\end{aligned}\tag{11}$$

where λ_1, λ_2, λ_3, and λ_4 denotes the singular points in the integral calculation.

By applying the residue theorem, the integral from equation (7) can be evaluated as follows:

$$\int_{-\infty}^{\infty}\left|H_1\right|^2 d\lambda=2\pi\mathrm{i}\sum\mathrm{Res}\left[\left|H_1\right|^2,\lambda_i\right]=2\pi\mathrm{i}\sum_{i=1}^{4}\lim_{\lambda\longrightarrow i\lambda_i}\left[(\lambda-i\lambda_i)\left|H_1\right|^2\right]=\pi\frac{C_4-2C_2B_2+C_0B_0^2}{D},\tag{12}$$

where

$$\begin{cases}D=\lambda_1\lambda_2\lambda_3\lambda_4\left(\lambda_2^2-\lambda_1^2\right)\left(\lambda_3^2-\lambda_1^2\right)\left(\lambda_4^2-\lambda_1^2\right)\left(\lambda_3^2-\lambda_2^2\right)\left(\lambda_4^2-\lambda_2^2\right)\left(\lambda_4^2-\lambda_3^2\right),\\C_0=\lambda_2\lambda_3\lambda_4\left(\lambda_3^2-\lambda_2^2\right)\left(\lambda_4^2-\lambda_2^2\right)\left(\lambda_4^2-\lambda_3^2\right)-\lambda_1\lambda_3\lambda_4\left(\lambda_3^2-\lambda_1^2\right)\left(\lambda_4^2-\lambda_1^2\right)\left(\lambda_4^2-\lambda_3^2\right)\\+\lambda_1\lambda_2\lambda_4\left(\lambda_4^2-\lambda_2^2\right)\left(\lambda_4^2-\lambda_1^2\right)\left(\lambda_2^2-\lambda_1^2\right)-\lambda_1\lambda_2\lambda_3\left(\lambda_3^2-\lambda_1^2\right)\left(\lambda_2^2-\lambda_1^2\right)\left(\lambda_3^2-\lambda_2^2\right),\\C_2=-\lambda_1^2\lambda_2\lambda_3\lambda_4\left(\lambda_3^2-\lambda_2^2\right)\left(\lambda_4^2-\lambda_2^2\right)\left(\lambda_4^2-\lambda_3^2\right)+\lambda_2^2\lambda_1\lambda_3\lambda_4\left(\lambda_3^2-\lambda_1^2\right)\left(\lambda_4^2-\lambda_1^2\right)\left(\lambda_4^2-\lambda_3^2\right)\\-\lambda_3^2\lambda_1\lambda_2\lambda_4\left(\lambda_4^2-\lambda_2^2\right)\left(\lambda_4^2-\lambda_1^2\right)\left(\lambda_2^2-\lambda_1^2\right)+\lambda_4^2\lambda_1\lambda_2\lambda_3\left(\lambda_3^2-\lambda_1^2\right)\left(\lambda_2^2-\lambda_1^2\right)\left(\lambda_3^2-\lambda_2^2\right),\\C_4=\lambda_1^4\lambda_2\lambda_3\lambda_4\left(\lambda_3^2-\lambda_2^2\right)\left(\lambda_4^2-\lambda_2^2\right)\left(\lambda_4^2-\lambda_3^2\right)-\lambda_2^4\lambda_1\lambda_3\lambda_4\left(\lambda_3^2-\lambda_1^2\right)\left(\lambda_4^2-\lambda_1^2\right)\left(\lambda_4^2-\lambda_3^2\right)\\+\lambda_3^4\lambda_1\lambda_2\lambda_4\left(\lambda_4^2-\lambda_2^2\right)\left(\lambda_4^2-\lambda_1^2\right)\left(\lambda_2^2-\lambda_1^2\right)-\lambda_4^4\lambda_1\lambda_2\lambda_3\left(\lambda_3^2-\lambda_1^2\right)\left(\lambda_2^2-\lambda_1^2\right)\left(\lambda_3^2-\lambda_2^2\right).\end{cases}\tag{13}$$

The common divisor $C_d=(\lambda_1-\lambda_2)(\lambda_1-\lambda_3)(\lambda_1-\lambda_4)(\lambda_2-\lambda_3)(\lambda_2-\lambda_4)(\lambda_3-\lambda_4)$ occurred in the above equations of coefficient D, C_0, C_2, and C_4. With the help of algebraic operation, the internal connections are given by

$$\begin{cases}X_0X_1X_2X_3-X_0^2X_1^2-X_0X_3^2=\dfrac{D}{C_d},\\X_0X_3=\dfrac{C_4}{C_d},\\X_0X_1=\dfrac{C_2}{C_d},\\X_1X_2-X_3=\dfrac{C_0}{C_d},\end{cases}\tag{14}$$

where

$$\begin{cases}X_0=\lambda_1\lambda_2\lambda_3\lambda_4,\\X_1=\lambda_1+\lambda_2+\lambda_3+\lambda_4,\\X_2=\lambda_1\lambda_2+\lambda_1\lambda_3+\lambda_1\lambda_4+\lambda_2\lambda_3+\lambda_2\lambda_4+\lambda_3\lambda_4,\\X_3=\lambda_1\lambda_2\lambda_3+\lambda_1\lambda_2\lambda_4+\lambda_2\lambda_3\lambda_4+\lambda_1\lambda_3\lambda_4.\end{cases}\tag{15}$$

The integral can be further derived as follows:

$$I_2=\int_{-\infty}^{\infty}\left|H_1\right|^2 d\lambda=\pi\frac{X_0X_3-2B_2^2(X_0X_1)+(X_1X_2-X_3)B_0^2}{X_0X_1X_2X_3-X_0^2X_1^2-X_0X_3^2}.\tag{16}$$

Moreover, relationships between complex singular points corresponding to the form of decompose and original denominator in (11) are given as follows:

$$\begin{cases}(i\lambda_1)^2(i\lambda_2)^2=A_2+A_3i,\\(i\lambda_1)^2+(i\lambda_2)^2=A_1+A_4i,\\(i\lambda_3)^2(i\lambda_4)^2=A_2-A_3i,\\(i\lambda_3)^2+(i\lambda_4)^2=A_1-A_4i.\end{cases}\tag{17}$$

Furthermore, the inner connection of singular points can be expressed as follows:

$$\begin{cases} \lambda_1\lambda_2\lambda_3\lambda_4 = \sqrt{A_2^2 + A_3^2}, \\ \lambda_1 + \lambda_2 = \sqrt{-(A_1 + A_4 i) - 2\sqrt{A_2 + A_3 i}}, \\ \lambda_3 + \lambda_4 = \sqrt{-(A_1 - A_4 i) - 2\sqrt{A_2 - A_3 i}}. \end{cases} \tag{18}$$

Substituting the relationships of singular points in equation (16) and mathematical transformation on the complex plane provided in the Appendix, the connections for singular points are derived as follows:

$$\begin{cases} X_0 = \sqrt{A_2^2 + A_3^2}, \\ X_1 = \sqrt{2}\sqrt{\sqrt{a^2 + b^2} - a}, \\ X_2 = \dfrac{\left(X_1^2 + 2A_1\right)}{2}, \\ X_3 = \dfrac{\left[X_2^2 + 2X_0 - \left(A_1^2 + A_4^2 + 2A_2\right)\right]}{2X_1}, \end{cases} \tag{19}$$

where

$$\begin{cases} a = A_1 + \sqrt{2}\sqrt{\sqrt{A_2^2 + A_3^2} + A_2}, \\ b = A_4 + \sqrt{2}\sqrt{\sqrt{A_2^2 + A_3^2} - A_2}, \end{cases} \tag{20}$$

Therefore, the integral of the square of FRF can be expanded as follows:

$$I_2 = \int_{-\infty}^{\infty} |H_1|^2 d\lambda = 8\pi \frac{X_1}{X_0} \frac{\left[4A_4^2X_0 - X_0{X_1}^4 - 8{X_0}^2 + 8A_2X_0 - 4A_1X_0{X_1}^2 + 16X_0{X_1}^2B_2 + B_0^2\left(8X_0 - 8A_2 - 4A_4^2 - 3{X_1}^4 - 4A_1{X_1}^2\right)\right]}{64A_2^2 + 64A_2A_4^2 + 16A_4^4 - 64A_4^2X_0 - 128A_2X_0 + 64{X_0}^2 + {X_1}^4\left(8A_4^2 + 16A_2 - 16A_1^2 + 48X_0\right) - 16A_1{X_1}^6 - 3{X_1}^8}. \tag{21}$$

An error analysis was performed to evaluate the correctness of equation (18) with the numerical discrete integral of $2\sum|H_1|^2$ from $\lambda = 0$ to $\lambda = 10$. Among these ranges, the useful and important frequency response factors in the calculation of the frequency response function for a two-degree of freedom system are collected, while the rest of the summation calculation from $\lambda = 10$ to $\lambda = \infty$ results in close to zero. Owing to the monotonicity of optimal parameters, the branch-and-bound algorithm was adopted. The step size of the variable parameters is determined by the accuracy of the optimal parameters for HD-TMD during the operation of numerical searching. The optimal parameters of HD-TMD had been acquired and corrected to four significant digits, which is enough in the application of civil engineering. As demonstrated in Figures 3(a)–3(c), the exact expression results were 100% matched with the data of discrete integral. Thus, it can be concluded that the simplification of the infinite integral through the residue theorem was successful.

3.2. Numerical Solutions. Normally, the simultaneous bivariate inhomogeneous equations of $\begin{cases} (\partial I_2/\partial f) = 0 \\ (\partial I_2/\partial \eta) = 0 \end{cases}$ should be taken as the next step toward the closed-form solutions for the optimal parameters of the HD-TMD. However, it is difficult to solve because of the theorem of Ruffini–Abel, which states that there is no explicit algebraic analytic solution for an order of the algebraic equation higher than 5. In this case, the maximum order of f is 7 in the numerator of I_2, not to mention that the order of f after partial derivatives (whose highest order is up to 14) that affect by the maximum order of f in the denominator. Hence, the numerical curve fitting technique was applied to acquire the expressions of optimal frequency and optimal HD ratio as follows:

$$\begin{cases} f_{opt} = p_1{\mu_t}^3 + p_2{\mu_t}^2 + p_3\mu_t + p_4, \\ \eta_{opt} = q_1{\mu_t}^{q_2}, \end{cases} \tag{22}$$

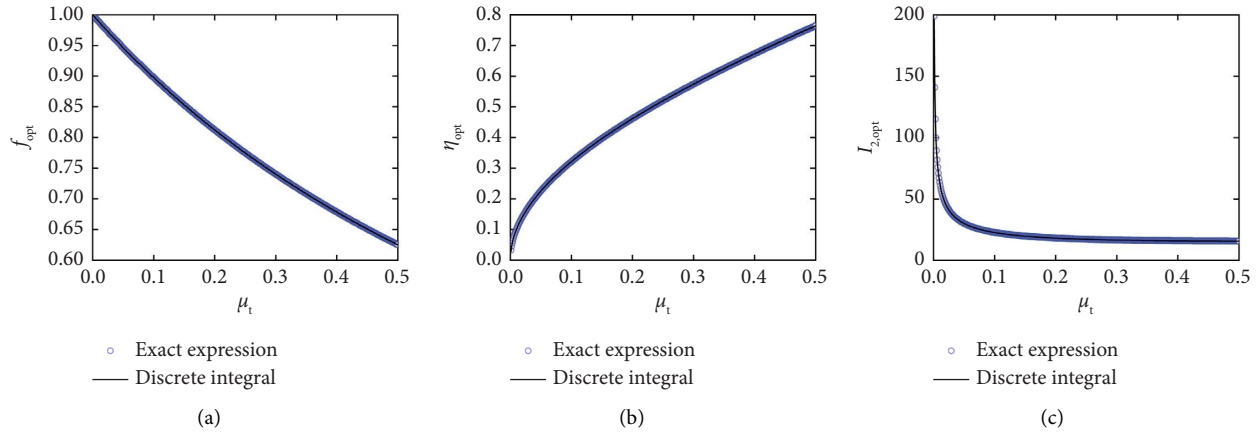

Figure 3: The correctness of applying the residue theorem. (a) Optimal frequency ratio. (b) Optimal damping ratio. (c) Optimal performance index.

where

$$\begin{cases} p_1 = -0.4776, \\ p_2 = 0.9573, \\ p_3 = -1.109, \\ p_4 = 1, \end{cases} \qquad \begin{cases} q_1 = 1.098, \\ q_2 = 0.5352. \end{cases} \tag{23}$$

Curve fitting results and comparisons are shown in Figures 4(a)–4(c). Data analysis showed that the maximum error and root square error of curve fitting compared to equation (21) were 0.1404% and 0.0349%, respectively, at the optimal frequency ratio. 6.631% and 1.6190% of the above errors occurred at an optimal HD ratio. The numerical solutions from equation (22) were curve-fitted between the mass ratios of 0% and 50%, which covered most of the HD-TMD working scenarios in practice. It can be easily concluded that the optimal frequency ratio and the performance index decreased with the rise of the mass ratio, whereas the optimal HD ratio increased.

By equating the damping energy of the HD-TMD and traditional viscous TMD in a resonate state [24, 25] with the same stroke, one of the relationships between the HD ratio and viscous damping ratio can be obtained as follows:

$$\begin{aligned} E_{D,HD} &= E_{D,viscous} \\ 2k_t \eta_{opt} x_t^{\,2} &= 2\pi k_t \xi_{opt} x_t^{\,2} \\ \eta_{opt} &= \pi \xi_{opt}. \end{aligned} \tag{24}$$

To emphasize the novelty of the proposed solution, comparisons with the solutions of Den Hartog, Warburton [6] (Page 385, Table 2, Case 5), and Xiang et al. [28] (Page 6, Table 3, Case 1) were performed, as shown in Figure 4. The frequency ratio exhibited an average value between those of Den Hartog and Warburton. It was observed that the proposed optimal numerical solution for the HD ratio is characterized by a lower value, whereas the effective HD ratio transferred by equation (24) was higher. Figure 4(c) exhibited that the H_2 optimization for HD-TMD was capable of minimizing the total vibration frequency energy of the structure while other classical theories were shown to be less effective. Results from Figure 4(c) indicated that the use of energy balance equivalence method such as equation (24) to optimize the structure-HD-TMD system is not feasible (shown subsequently in the numerical verification section). The comparisons between H_∞ optimization [28] and H_2 optimization for HD-TMD were conducted. For different optimal criteria, the optimal parameters of HD-TMD appeared distinct differences, where the optimal frequency ratio derived from fixed-point theory is lower than the proposed optimal frequency ratio and the former optimal hysteretic damping ratio is higher than the latter one. The performance index of H_2 optimization was 2.349% and 2.2052% lower than the H_∞ optimization in respect of maximum difference and average difference.

The potential meanings of the proposed H_2 optimization for HD-TMD are the original mathematical derivation guidance for this type of infinite integral in math and the precious time that can be saved by applying this simplification to eliminate a further dimension search in the frequency domain.

The detailed procedure for H_2 optimization for HD-TMD was summarized in Figure 5. To provide a significant difference between the H_2 optimization for HD-TMD and the traditional viscous TMD, the detailed procedure for H_2 optimization for traditional viscous TMD was summarized in Figure 6. It can be observed that except for the basic principle of the residue theorem, relationships of the coupled complex solutions and associated expressions with the original coefficient are reformed in the H_2 optimization for HD-TMD, which exposed the complexity in math. The step-by-step derivation of H_2 optimization for HD-TMD is not only the expression of the complexity of math but also provides a precious and original process for solving the simplification of the infinite integral of HD-TMD (or any kind of systems, whose square calculation of the

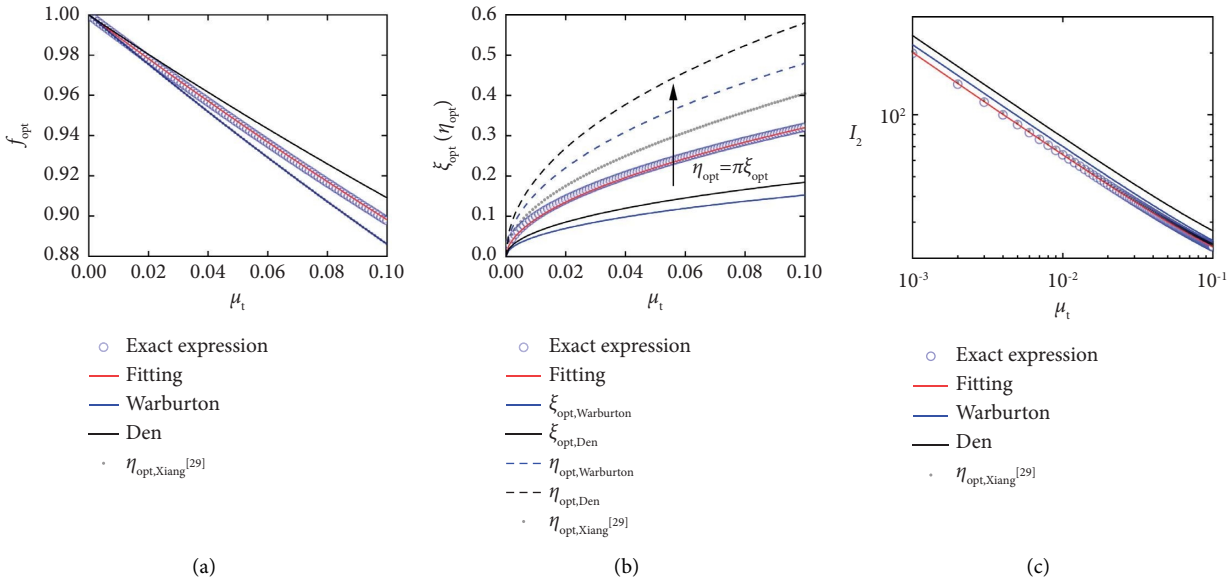

Figure 4: Curve fitting applied for H_2 theory of structure with HD-TMD system. (a) Optimal frequency ratio. (b) Optimal damping ratio. (c) Optimal performance index.

Table 2: Parameters for the traditional TMD and HD-TMD.

TMD types	α	f_{opt}	$\xi_{t,opt}$	η_{opt}	Named
Warburton's TMD	—	0.9636	0.08566	—	TMD1
Warburton's HD-TMD	—		—	0.2691	TMD2
H_2 optimized HD-TMD	0	0.9676	—	0.1681	TMD3
Performance balance design HD-TMD	2.377%	0.9676	—	0.2385	TMD4
Matta's HT-BTMD	—	0.9807		0.3314	TMD5

Table 3: Optimization cases for damped SDOF structure with HD-TMD systems.

Names	R_{max} (%)	$R_{RMS,quake}$ (%)	$\lvert x_t\rvert_{max}$ (m)	$\lvert\ddot{x}_1+\ddot{x}_g\rvert_{max}$ (m/s^2)	Maximum base shear force (kN)	$\lvert F_D\rvert_{max}$ (kN)	Maximum damping energy (kJ)	Maximum pendulum rotation angle (°)
Uncontrol	100.000	100.000	—	0.428	3592.5	—	—	—
TMD1	68.278	54.915	1.486	0.348	2968.5	0.558	813.3	—
TMD2	71.405	57.428	1.413	0.360	3035.8	0.908	823.1	7.424
TMD3	68.601	54.094	1.685	0.353	2975.5	0.694	832.1	8.940
TMD4	71.449	57.803	1.397	0.360	3036.7	0.912	823.5	7.403
TMD5	72.993	60.888	1.237	0.363	3069.3	1.008	807.9	6.727

FRFs can be expressed as equation (9)) that no one has completed before.

4. Performance Balance Design for HD-TMD

The previous H_2 optimization mentioned provides the optimal parameters without concerning the working condition for HD-TMD. However, in high-rise buildings, the movement of TMD is restrained within a certain range, where the space utilization rate and economic benefit of the structure will be thereby greatly improved. Consequently, to solve this problem at the design level, a performance balance design considering the movement of HD-TMD was carried out by adjusting the weighting factor. The relevant parametric study was presented subsequently.

4.1. Performance Index with the Weighting Factor. A performance index with a percentage weighting factor α in equation (25) was inspired by Wang et al. [29] to illustrate the further mechanism of displacement limitation of HD-TMD. It can be observed that the priority of the minimum structure response is thereby decreased by the weighting factor, and the consideration of TMD

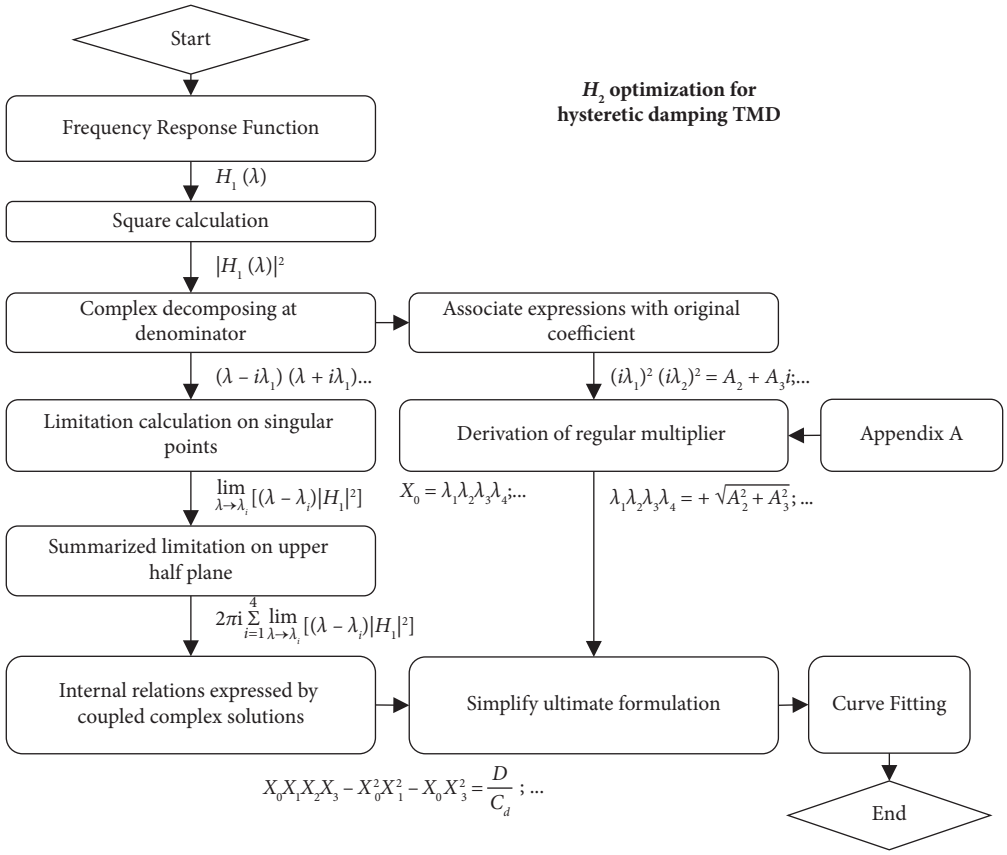

Figure 5: Procedure for H_2 optimization of HD-TMD.

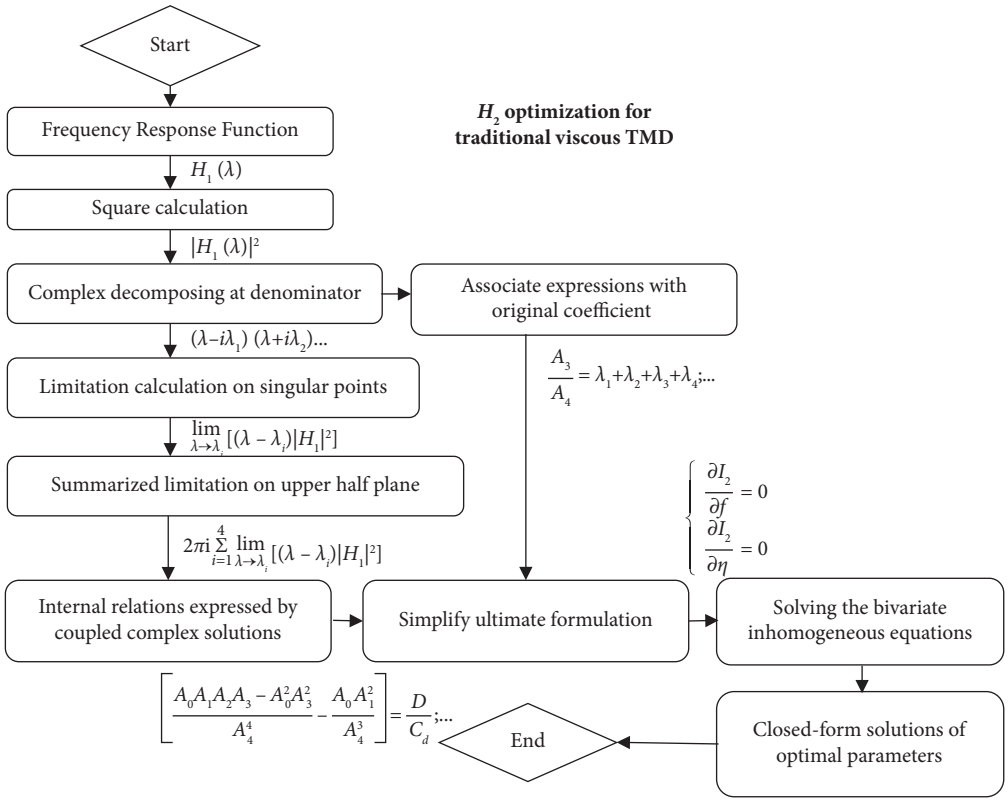

Figure 6: Procedure for H_2 optimization of traditional viscous damping TMD.

response is taken into account at the same time. Participation in the weighting factor leads to a trade-off problem. It can be seen as an estimation of desired performance that balances with the response of structure and TMD.

$$I_1 = (1-\alpha)I_2 + \alpha I_3, \tag{25}$$

where $I_2 = \sigma_1^2/S_0$, $I_3 = \sigma_t^2/S_0 = \int_{-\infty}^{\infty} |H_t|^2 d\lambda$, and $\alpha \in [0, 100\%)$. By introducing $\xi_1 = 0$, the expression of I_3 from equation (5) was given by

$$\left|H_t(i\lambda)\right|^2 = \frac{1}{\left[\lambda^4 - \lambda^2(A_1 + iA_4) + A_2 + iA_3\right]\left[\lambda^4 - \lambda^2(A_1 - iA_4) + A_2 - iA_3\right]}. \tag{26}$$

Similarly, the infinite integral of I_3 can be simplified using the residue theorem as Section 3.1 had performed and demonstrated as follows:

$$I_3 = \int_{-\infty}^{\infty} \left|H_t\right|^2 d\lambda = 2\pi \mathrm{i} \sum \mathrm{Res}\left[\left|H_t\right|^2, \lambda_i\right] = 2\pi \mathrm{i} \sum_{i=1}^{4} \lim_{\lambda \longrightarrow i\lambda_i} \left[(\lambda - i\lambda_i)\left|H_t\right|^2\right] = \pi \frac{C_0}{D}, \tag{27}$$

which can be further obtained as follows:

$$I_3 = \int_{-\infty}^{\infty} \left|H_t\right|^2 d\lambda = \pi \frac{X_1X_2 - X_3}{X_0X_1X_2X_3 - X_0^2X_1^2 - X_0X_3^2}. \tag{28}$$

Therefore, the performance index for performance balance design with weighting factor can be expressed as follows:

$$I_1 = \pi \frac{(1-\alpha)\left(X_0X_3 - 2B_2^2(X_0X_1) + (X_1X_2 - X_3)B_0^2\right) + \alpha(X_1X_2 - X_3)}{X_0X_1X_2X_3 - X_0^2X_1^2 - X_0X_3^2}, \tag{29}$$

where coefficients refer to equation (19).

4.2. Parametric Study. To further investigate the variation of α, the double Y axes plots of f_{opt} and η_{opt} for different mass ratios of 0.5%, 1%, 2%, and 10% are drawn in Figure 7 based on the numerical searching strategy. The optimal frequency ratio remained stable with weighting factors ranging from 0% to 5%, while the optimal HD ratio increased with the increase of the weighting factor. The optimal frequency ratio and HD ratio held the same patterns with the variate of the weighting factor for different mass ratios as previously discussed in Section 3.2 and Figure 4, which were demonstrated in blue solid and red dashed lines. The maximum difference of the optimal HD ratio was 17.1% for mass ratio equal to 0.5% and 9.4% for mass ratio equal to 10%. It should be noted that the optimal HD ratio was more sensitive to the weighting factor for a small mass ratio of HD-TMD.

The corresponding performance indexes for the performance balance design of HD-TMD are shown in Figure 8. As seen from Figure 8, performance indexes were positively related to the weighting factor, indicating that the control performance of HD-TMD weakened owing to the percentage consideration of the response of HD-TMD itself. In addition, the performance indexes for small mass ratios HD-TMD were more sensitive to the weighting factor than those of the large mass ratios. Meanwhile, I_1 variate a lot from the I_2 with the increase of weighting factor thanks to the contribution of I_3.

Owing to the positive growth of the structural performance index, the undesired control loss must be constrained. As a further illustration of the physical significance of the weighting factor, a tolerance ratio of structural response was proposed for judging the acceptable rate of deviation from the H_2 optimization.

The optimal performance index for performance balanced design in terms of mass ratio of HD-TMD equal to 3% was presented as an example in Figure 9. It was found that the tolerance ratios provided several boundary conditions for restraining the growth of the performance index. The undesired control loss was indicated clearly with the red line, where corresponding optimal HD ratios and weighting factors were noted. The tolerance ratio based on the structural displacement reflected the conditions of using performance balance design, which should be limited between the contribution of the movement of TMD and the acceptable control loss for the structural response.

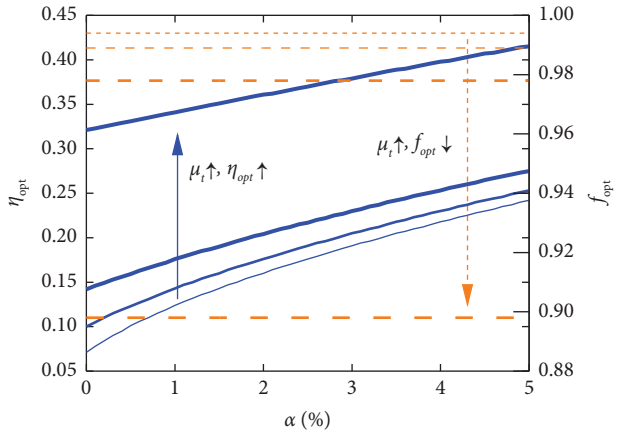

FIGURE 7: Optimal parameters for HD-TMD based on performance balance design (dashline: optimal frequency ratio, solidline: optimal HD ratio).

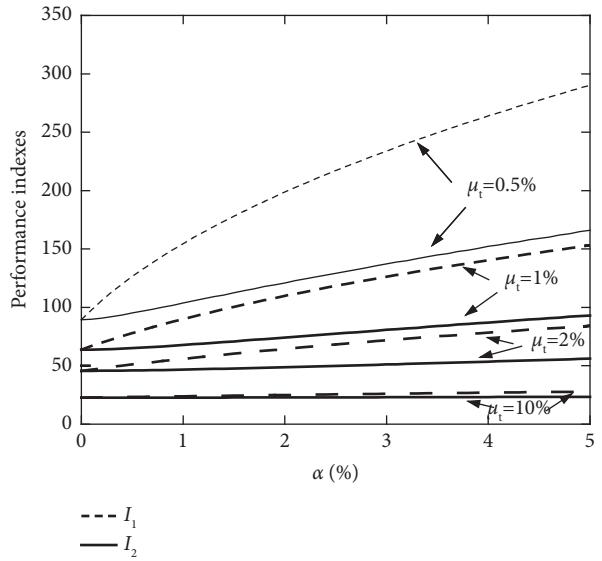

FIGURE 8: Optimal performance indexes for performance balance design.

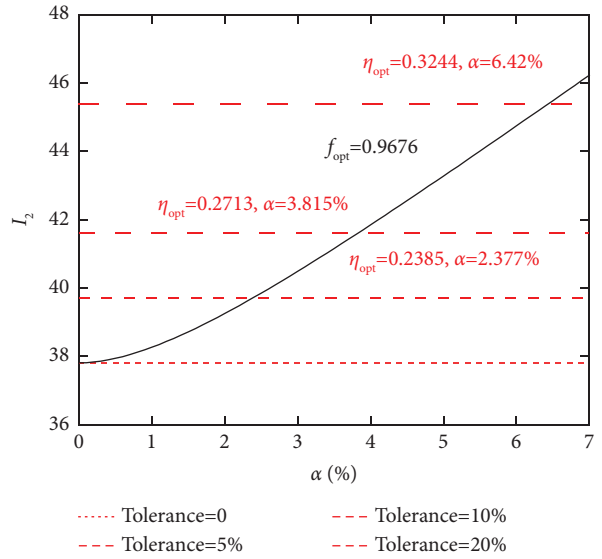

FIGURE 9: Optimal performance index for performance balance design of μ_t = 0.03.

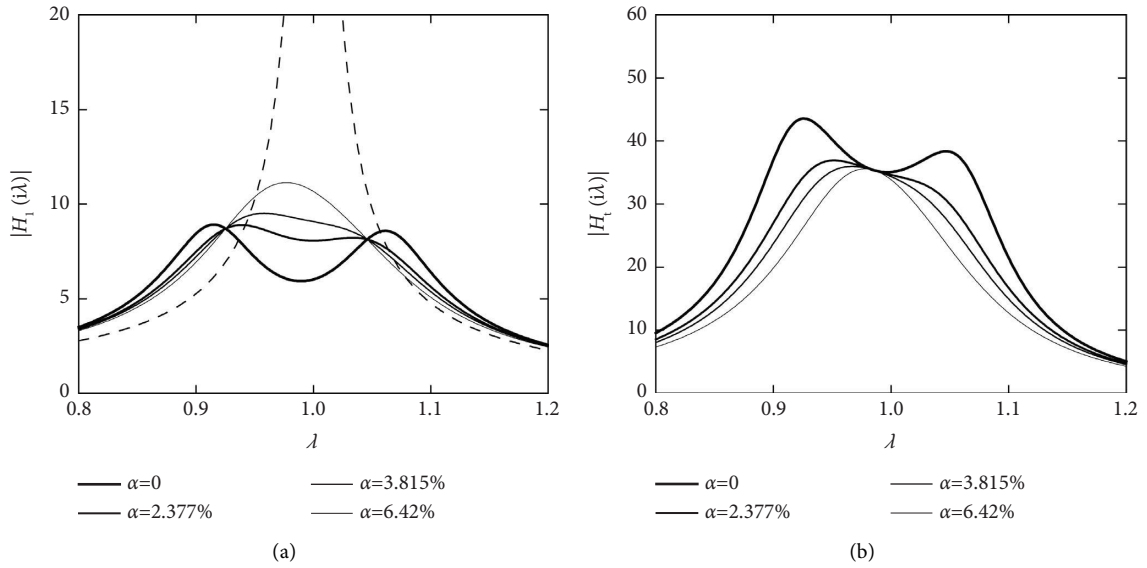

Figure 10: The DAFs for displacement response of $\mu_t = 0.03$. (a) Structure and (b) HD-TMD.

To analyze the difference between FRFs, the dynamic amplification factors (DAFs) that represent the absolute value of FRFs were compared in Figures 10(a) and 10(b). It should be noted that specific weighting factors were adopted based on the tolerance ratio management for the performance index of structure response. It was demonstrated that the DAFs for the structure and HD-TMD were perfectly tuned to the double peak curve shape, and the peaks for the structure were almost the same. However, as the weighting factor increased, the peak of structural DAFs increased, representing the appearance of control loss, whereas the peak of HD-TMD decreased, meaning the relative absence of the HD-TMD response. Moreover, it can be observed that the overall values of DAFs for HD-TMD were several times higher than those for structure, suggesting that the difference in the performance indexes that accounts for the DAFs was larger. Thus, the weighting factor should be carefully used; otherwise, it may come out with a meaningless result.

It is well known that the frequency ratio of TMD determines the energy absorption efficiency from the structure, which was shown to be more significant than the damping ratio [38]. Therefore, considering the frequency ratio detuned from the design, the detuning effect of HD-TMD is shown in Figure 11. It was observed that the performance index of the structural response increased rapidly when the detuning factor was equal to zero. The robustness of the HD-TMD was greatly improved by the performance balance design, which was attributed to the corresponding increase in the HD ratio.

The procedure for the performance balance design of HD-TMD was described in Figure 12. It should be noted that the procedure mentioned in this study provided a tolerance ratio that allows designers to accurately adjust the performance for the structure with the HD-TMD system, rather than the uncertain concept of a weighting factor in the previous studies.

5. Numerical Verifications

Owing to the hypothesis of white-noise seismic excitations, the detailed performance of the optimal parameters for HD-TMD needs to be further analyzed via natural earthquake records and harmonic excitations. Here, VFP-TMD [23], as a nonlinear real application and illustration for the optimal design of HD-TMD, was selected to examine the optimal numerical solutions and performance balance design for HD-TMD.

5.1. Linear Comparisons. Twenty sets of real earthquake acceleration records on the site class C that were recommended by ATC-40 [39] were used in time-history analysis with the same peak ground acceleration of 0.2 g for structures equipped with the regular TMD and HD-TMD. Assuming that the inherent damping ratio of the primary structure was $\xi_1 = 0.02$, the TMD mass ratio was $\mu_t = 0.03$, and the optimal design parameters for traditional TMD and HD-TMD were obtained using the optimal numerical solutions and performance balance design with a tolerance ratio equal to 5%, as listed in Table 2. Based on the same random theory, the optimal closed-form solutions derived by H_2 optimization from Warburton [6] (Page 385, Table 2, Case 5) for traditional TMD and the corresponding effective HD ratio for HD-TMD transferred by (24) were compared in this section. The numerical calculation was operated by the Newmark-β method [40].

The mean responses for 20 sets of earthquake records are shown in Figures 13(a) and 13(b). It can be inferred that both traditional TMD and HD-TMD exhibited excellent and stable displacement mitigation capacity on displacement for flexible structures with periods over 1 second. Moreover, the proposed optimal numerical solutions based on H_2 optimization demonstrated better performance in displacement

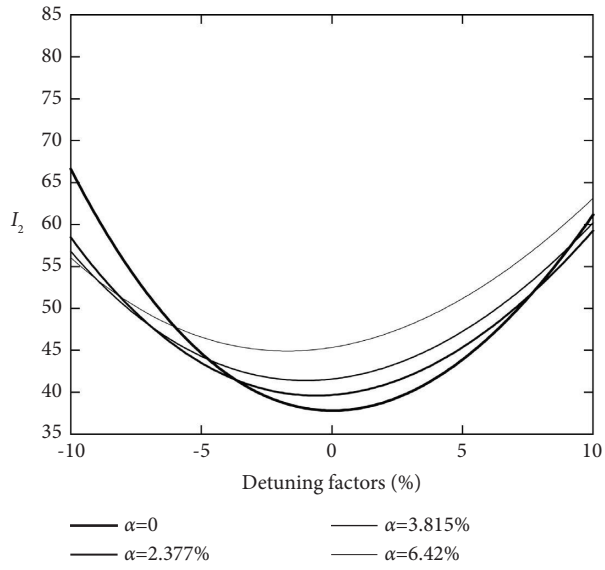

FIGURE 11: Detuning effect for performance balance design of $\mu_t = 0.03$.

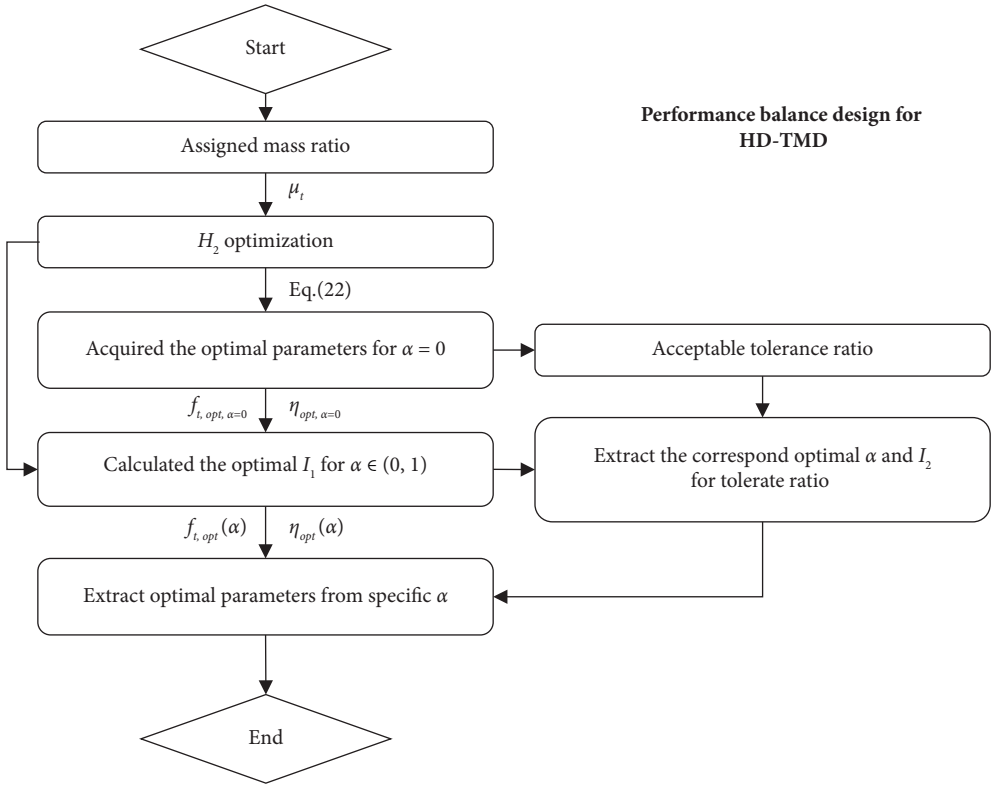

FIGURE 12: Procedure for performance balance design.

response. For the relatively flexible structures whose period approaches 6 seconds, the proposed TMD3 and TMD4 reflected the advantages of structure displacement control. It can be seen from Figure 13(b) that the maximum acceleration reduction was limited for those structural periods of more than 1.7 s. Moreover, the constant superiority of the proposed optimized HD-TMD for multiple structural periods was illustrated, implied the further beneficial structural control features against a wider set of different structural frequency modes of HD-TMD.

For a specific structural analysis, the natural period of the main structure $T_1 = 6.397s$, the inherent damping ratio of the primary structure $\xi_1 = 0.02$, and the TMD mass ratio $\mu_t = 0.03$ were considered [41]. Matta [24] summarized the

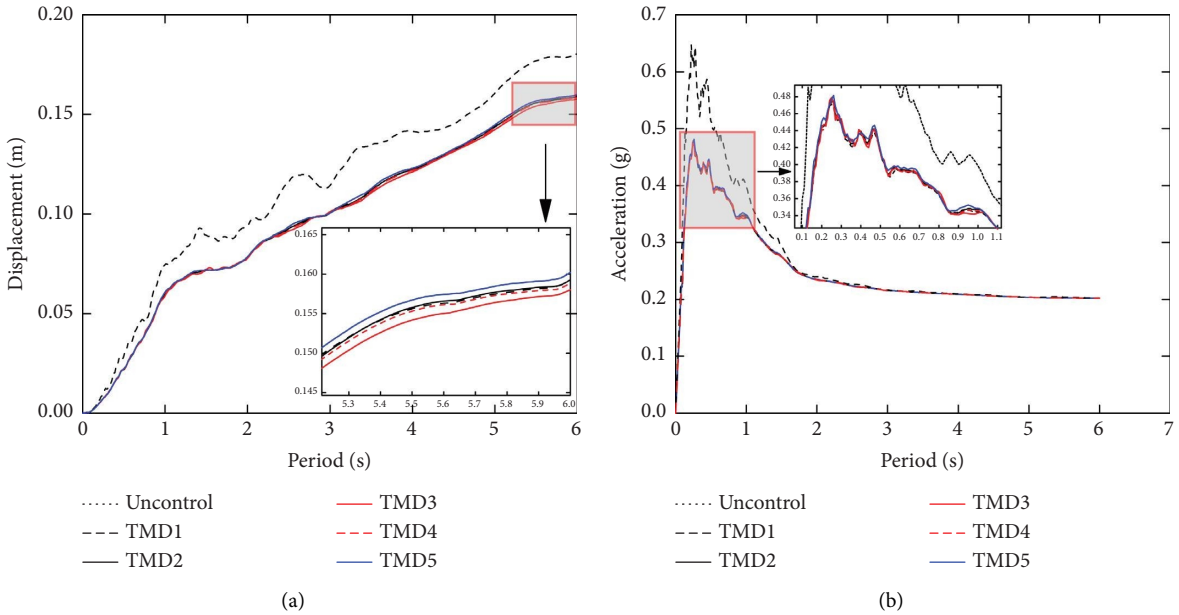

FIGURE 13: Structural mean response spectrum for 20 sets of earthquake records. (a) Maximum displacement response. (b) Maximum acceleration response.

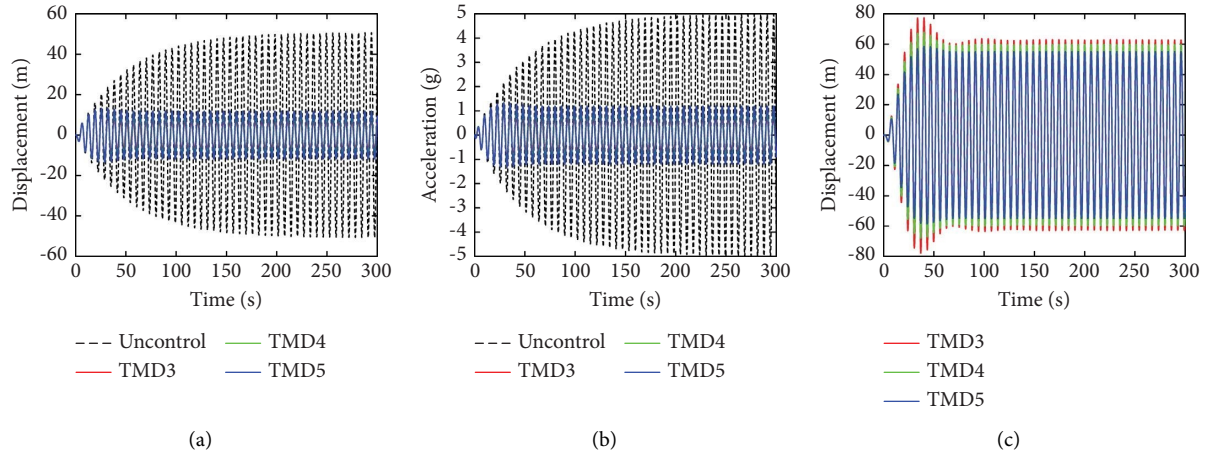

FIGURE 14: Numerical verification of the resonate harmonic excitation. (a) Structural displacement response. (b) Structural acceleration response, and (c) HD-TMD displacement response.

numerical optimal parameters of linear HT-BTMD based on H_∞ optimization for the above structure, which are listed in Table 3 and compared in the following verifications. Without loss of generality, the performance balance design was chosen to validate the effectiveness of a tolerance ratio of 5%.

As shown in Figures 14(a)–14(c), the proposed HD-TMD optimized by H_2 optimization, performance balance design, and Matta exhibited stable mitigation capacity on displacement and acceleration against accelerated excitation, where reduction rates were 14.07%, 18.53%, and 23.42% for the structural displacement and 14.24%, 19.4%, and 23.93% for the structural acceleration, respectively. The above data suggested that the proposed optimal numerical solutions exhibit the most impressive vibration reduction ability. Meanwhile, the structural response from the performance balance design increased from the results of the optimal numerical solutions but still performed better than the results from Matta.

5.2. Real Application Example. As mentioned in Section 2.1, the VFP-TMD fulfilled its functionalities through the pendulum movement of the TMD in the vertical plane and the variable friction arrangement that was successfully tested and applied in the isolated structures [42–44]. The equivalent constant stiffness force provided by the pendulum path is only available in the small displacement circumstances for the TMD

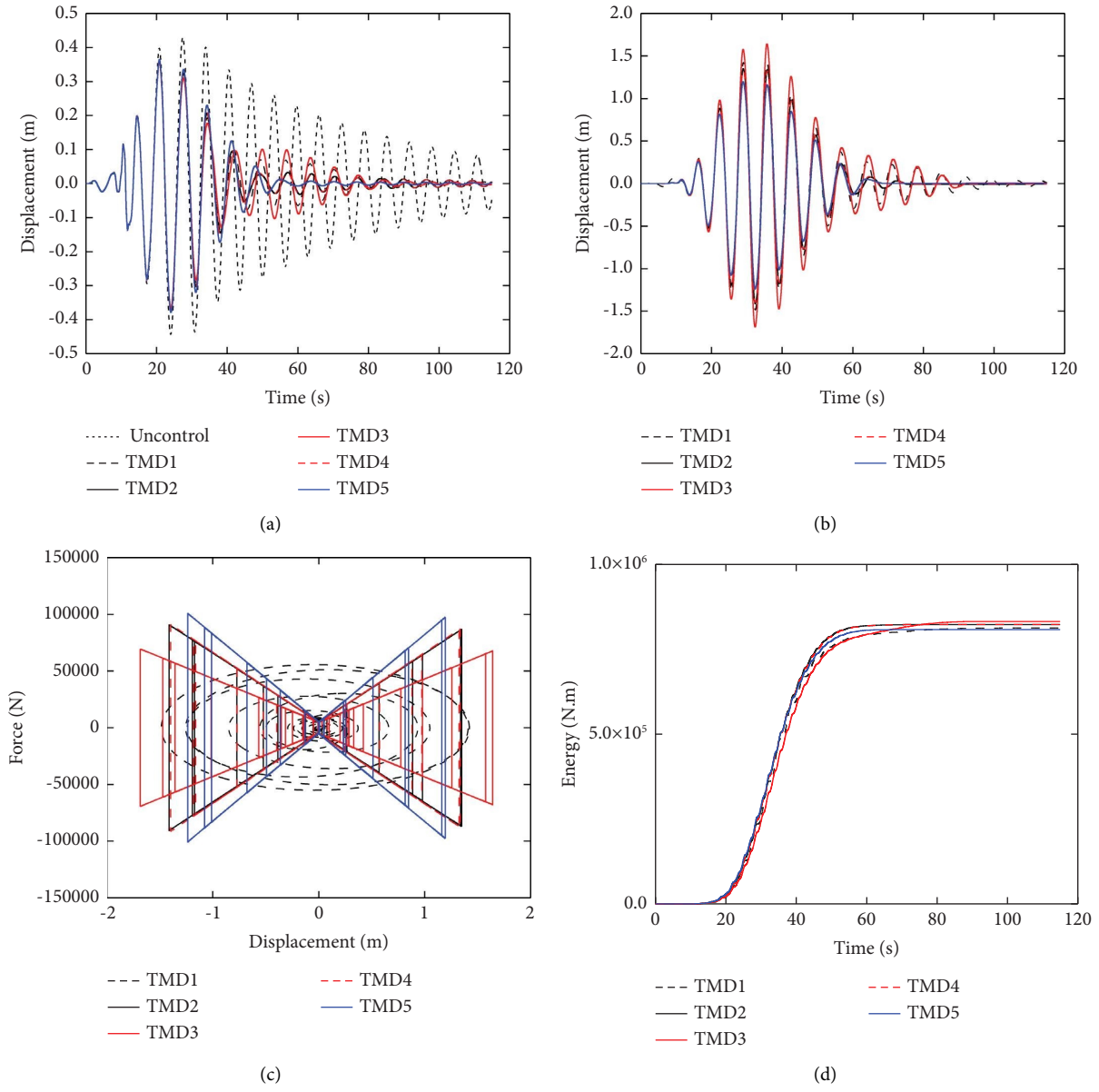

Figure 15: Numerical verification for earthquake excitation of SDOF structure. (a) Structural displacement response. (b) TMDs' displacement response. (c) Hysteretic loop for TMDs. (d) Damping energy of TMDs.

itself [45], which highlights the importance of working conditions for such kind of HD-TMD. The other significant friction nonlinear property of the VFP-TMD is its original friction force that is contributed by the initial interconnection with the surface of the TMD and the pendulum path, which alters the damping force of TMD as follows:

$$F_D = \operatorname{sign}(\dot{x}_t)\left(\eta k_t |x_t| + \mu_{\min} N_t\right), \tag{30}$$

where $\mu_{\min}$ stands for the original friction coefficient and the N denotes the gravity of the TMD. (30) transfers into constant friction damping force ($F_D = \operatorname{sign}(\dot{x}_t)\mu_{\min} N_t$) [46] when the hysteretic damping part is equal to zero ($\eta k_t |x_t| = 0$). The equations of motion for the structure with the VFP-TMD system are listed as follows [25]:

$$\begin{cases} (m_1 + m_t)\ddot{x}_1 + m_t\ddot{x}_t + c_1\dot{x}_1 + k_1 x_1 = -(m_1 + m_t)\ddot{x}_g, \\ m_t\ddot{x}_1 + m_t\ddot{x}_t + k_t x_t + F_D = -m_t\ddot{x}_g. \end{cases} \tag{31}$$

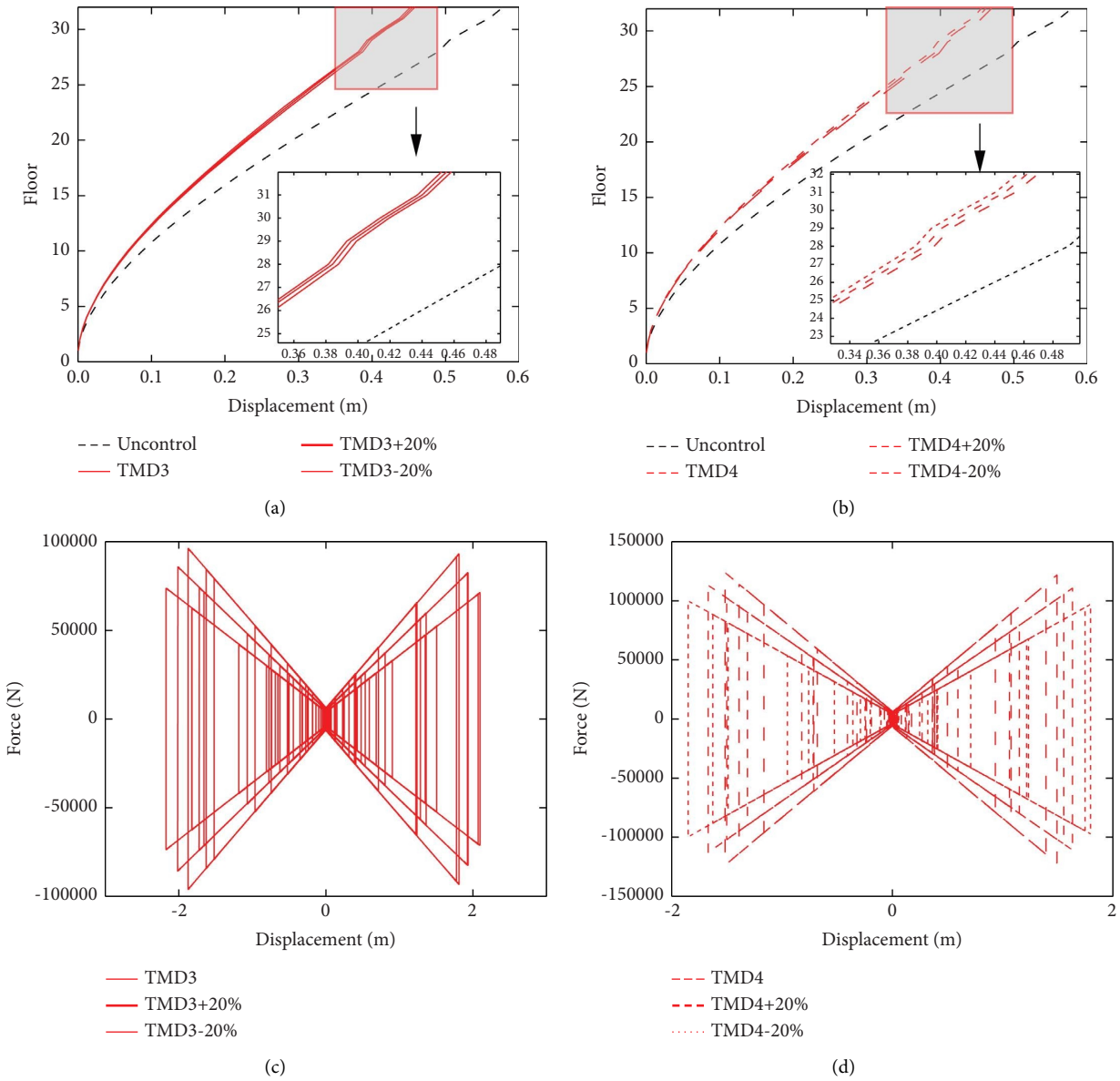

FIGURE 16: Numerical verification for earthquake excitation of MDOF structure. (a) The maximum structural displacements using TMD3. (b) The maximum structural displacements using TMD4. (c) Hysteretic loops for TMD3s. (d) Hysteretic loops for TMD4s.

Detailed information was needed for the nonlinear system based on the aforementioned parameters, which employed the first modal mass of the structure $m_1 = 8.4 \times 10^6 kg$, the gravity of the mass of TMD $N_t = 2.4696 \times 10^6$N [41]. The original friction coefficient was assumed to be $\mu_{\min} = 0.002$ as unavoidable friction coefficient on the surface of regular material. The time history analysis results of the structure with the VFP-TMD system under the Loma Prieta earthquake for $\mu_t = 0.03$ were prepared in Figures 15(a)–15(d), where the ground motion recorded on Yerba Buena Island was one of the selected ground motions mentioned before. To better illustrate the TMDs' performance during the earthquake excitation, the relative structural root mean square (RMS) reduction rate $R_{RMS,\text{quake}}$ and the maximum structural displacement reduction rate $R_{\max}$ were defined as $R_{\max} = x_{1,\max,TMD}/x_{1,\max,unc}$ and $R_{RMS,\text{quake}} = \sigma^2_{1,TMD}/\sigma^2_{1,unc}$, respectively. The data for detailed performance points are shown in Table 3.

It was evident that TMDs exhibit excellent mitigation capacity toward earthquake excitation, where TMD1 and TMD3 perform the best at $R_{\max}$, $R_{RMS,\text{quake}}$, maximum structural absolute acceleration $|\ddot{x}_1 + \ddot{x}_g|_{\max}$, and maximum structural base shear force. TMD1 was a theoretical and classical object for comparison, whose existing friction force in real application of viscous damping element was neglected. As shown in figure 15(d) and Table 3, the structural displacement RMS for TMD3 was the minimum value during earthquake excitation and the damping energy for TMD3 was the maximum value, indicating that the proposed H_2 optimization for HD-TMD can greatly suppress the vibration of the structure against earthquake excitation.

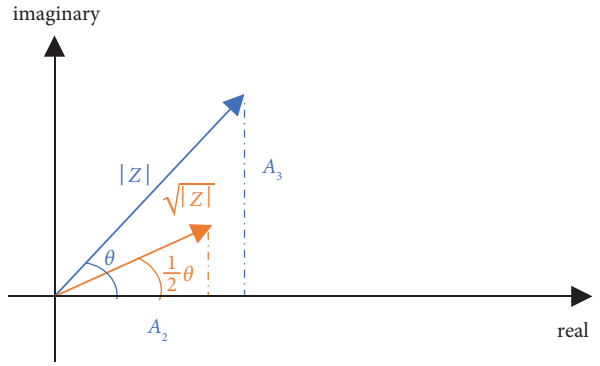

Figure 17: Plural decomposition in the first quadrant complex field.

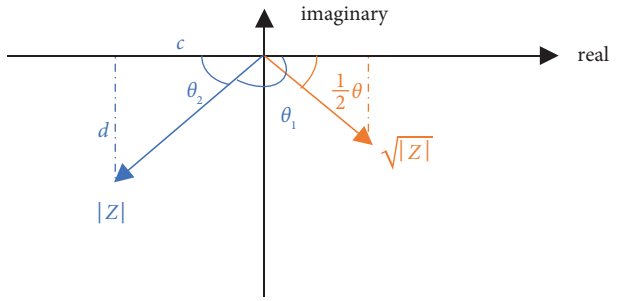

Figure 18: The plural decomposition in the third quadrant complex field.

One of the assumptions mentioned above states, that the working condition for the VFP-TMD is limited when it exhibits linear properties. Therefore, the performance balance design is vital to hold the linear property of VFP-TMD. As seen from Table 3, the maximum pendulum rotation angle of TMD3 was the maximum which was shown to barely hold the linear property according to Xu et al. (9°) [45], but the TMD4 results suggested that the performance balance design successfully reduced the maximum pendulum rotation angle of the VFP-TMD which ensured the linear property of the HD-TMD while providing impressive mitigation capacity to structure. It was found that after the performance balance design, there are 2.847% of loss in the maximum structural displacement reduction rate and 3.709% of loss in the RMS reduction rate during the earthquake-excited period, respectively. The results also indicated that the proposed methods for HD-TMD can be applied to lightly damped structures equipped with HD-TMD.

Additionally, the multidegree of freedom (MDOF) structural analysis combined with the degradation of friction coefficients of HD-TMD was illustrated as a preliminary analysis toward real application analysis. The MDOF structural model was referred from the literature [41]. In the reality, the tribological properties vary along the response of the device, with sliding velocity, normal pressure, and heating phenomena induced by the sliding itself [47, 48]. Here, considering a range of friction coefficient variations ± 20% was accessed to draw a rough analysis on the deviation of friction coefficient.

The analysis data of the MDOF structure is shown in Figures 16(a)–16(d). The maximum structural displacement was reduced significantly on the higher floors of the structure rather than the lower floors by the adopted optimized TMDs, which indicated the urgent need for the slender structure to deploy vibration suppression device and the successful application of HD-TMD to mitigate the earthquake hazard. Although the optimizations were proposed based on the undamped SDOF structure-HD-TMD system, the optimized HD-TMDs demonstrated stable and excellent structural control performance against a wider set of structural modes. The worst-case study of friction coefficient variations illustrated that the decrease of friction coefficient led to a slight improvement in the displacement performance while the increase of friction coefficient resulted in a worse performance but reduced the stroke of TMD, which reflected the same principle of the performance balance design as discussed.

6. Conclusions

In this study, the seismic optimization of HD-TMD subjected to white-noise excitation was conducted. The H_2 optimization was proposed to minimize the frequency energy based on the integral of FRF. Owing to the concern about the working condition for HD-TMD, performance balance design was carried out. Numerical verifications based on real HD-TMD applications were conducted to examine the correctness of the proposed methods, which demonstrated great advantages compared with the traditional methods. Several important conclusions can be drawn as follows:

(1) As a type of TMDs, the HD-TMD exhibits displacement-dependent damping force, which can be achieved by altering the friction-damping output. The equations of motion for the structure with the HD-TMD system were derived. Numerical validation was conducted for various excitation amplitudes, which exhibited the linear behavior for the HD-TMD. Furthermore, the frequency response functions of the structure with the HD-TMD system were presented.

(2) H_2 optimization for HD-TMD was derived cautiously and skillfully based on the simplified integral utilizing the residue theorem. The numerical integral results showed that simplification was 100% accurate. Due to the orders of the algebraic analytic solution was too high, the closed-form parameters solutions are not possible to solve due to the theorem of Ruffini–Abel. Numerical curve-fitting solutions for HD-TMD for the mass ratio between 0% and 50% were provided instead.

(3) With the help of the weighting factor, the performance balance design for HD-TMD was carried out. By slightly changing the performance index expression, the optimal performance for HD-TMD considering the movement of TMD is thereby achieved. The parametric study demonstrated that the weighting factor needed to be carefully chosen

with the help of the tolerance ratio to avoid physically meaningless results. The HD ratio of HD-TMD is more sensitive to the weighting factor than to the frequency ratio. The robustness of the HD-TMD was improved by the performance balance design.

(4) A set of earthquake records were used to statistically analyze the HD-TMD performance and generate average earthquake response spectrums. Results showed that both regular TMD and HD-TMD exhibited excellent and stable displacement mitigation capacity on displacement for flexible structures whose period was over 1 s. Harmonic excitations were conducted which proved the structural response for performance balance design increased from the results of the optimal numerical solutions but still performed well.

(5) For a real application example of HD-TMD, the VFP-TMD was selected to undergo earthquake excitation with parameters from optimal numerical solutions and performance balance design. The comprehensive indexes indicated that the optimal numerical solutions for HD-TMD can improve the structural response to the maximum extent. In this case, the maximum pendulum rotation angle was so large that the linear property was barely maintained. Fortunately, the performance balance design helped decrease the maximum pendulum rotation angle while providing impressive seismic mitigation capacity for the structure. Compared with optimal numerical solution results, the performance balance design demonstrated 2.847% of loss in maximum structural displacement reduction rate and 3.709% of loss in root mean square reduction rate during the earthquake-excited period, respectively.

Appendix

Mathematical transformation on the complex plane was conducted to eliminate the influence of the imaginary part of the combined complex formulation, which was numerically proven to result in a real number.

In Section 3.1, the coupled formulations of equation (16) are given as follows:

$$\lambda_1 + \lambda_2 + \lambda_3 + \lambda_4 = \sqrt{-(A_1 + A_4 i) - 2\sqrt{A_2 + A_3 i}} + \sqrt{-(A_1 - A_4 i) - 2\sqrt{A_2 - A_3 i}}. \tag{A.1}$$

As basic mathematical knowledge and the following mathematical transformation principle, a complex number with root calculation leads to a half-angle of the original one and root at the absolute length of the original one in the default geometric view of the complex plane as Figure 17.

First, simplification like $\sqrt{A_2 + A_3 i}$ can be derived as follows:

It can be seen from the above-mentioned figure, $\sqrt{A_2 + A_3 i} = \sqrt{|z|}\cos 1/2\theta + i\sqrt{|z|}\sin 1/2\theta$ that $\sqrt{|z|} = \sqrt{\sqrt{A_2^2 + A_3^2}}$, $\tan\theta = A_3/A_2$.

Using half-angle relations in trigonometric functions, relationships can be written as follows:

$$\begin{cases} \cos\dfrac{1}{2}\theta = \sqrt{\dfrac{1+\cos\theta}{2}} = \sqrt{\dfrac{1 + A_2/\sqrt{A_2^2 + A_3^2}}{2}} = \sqrt{\dfrac{\sqrt{A_2^2 + A_3^2} + A_2}{2\sqrt{A_2^2 + A_3^2}}}, \\ \sin\dfrac{1}{2}\theta = \sqrt{\dfrac{1-\cos\theta}{2}} = \sqrt{\dfrac{1 - A_2/\sqrt{A_2^2 + A_3^2}}{2}} = \sqrt{\dfrac{\sqrt{A_2^2 + A_3^2} - A_2}{2\sqrt{A_2^2 + A_3^2}}}. \end{cases} \tag{A.2}$$

Hence, the above relationships come out with

$$\sqrt{A_2 + A_3 i} = \frac{1}{\sqrt{2}}\left(\sqrt{\sqrt{A_2^2 + A_3^2} + A_2} + i\sqrt{\sqrt{A_2^2 + A_3^2} - A_2}\right). \tag{A.3}$$

Second, simplification like $\sqrt{-c-di}$ can be derived as follows, where

$$\begin{cases} c = A_1 + \sqrt{2}\sqrt{\sqrt{A_2^2 + A_3^2} + A_2} > 0, \\ d = A_4 + \sqrt{2}\sqrt{\sqrt{A_2^2 + A_3^2} - A_2} > 0. \end{cases} \tag{A.4}$$

It can be seen from Figure 18, $\sqrt{-c-di} = \sqrt{|z|}\cos 1/2\theta_1 - i\sqrt{|z|}\sin 1/2\theta_1$, where $\sqrt{|z|} = \sqrt{\sqrt{c^2+d^2}}$, $\tan\theta_2 = d/c$, and $\theta_2 + \theta_1 = \pi$.

Using half-angle relations in trigonometric functions, relationships can be written as follows:

$$\begin{cases} \cos\dfrac{1}{2}\theta_1 = \sqrt{\dfrac{1+\cos\theta_1}{2}} = \sqrt{\dfrac{1-\cos\theta_2}{2}} = \sqrt{\dfrac{1-c/\sqrt{c^2+d^2}}{2}} = \sqrt{\dfrac{\sqrt{c^2+d^2}-c}{2\sqrt{c^2+d^2}}}, \\ \sin\dfrac{1}{2}\theta_1 = \sqrt{\dfrac{1-\cos\theta_1}{2}} = \sqrt{\dfrac{1+\cos\theta_2}{2}} = \sqrt{\dfrac{1+c/\sqrt{c^2+d^2}}{2}} = \sqrt{\dfrac{\sqrt{c^2+d^2}+c}{2\sqrt{c^2+d^2}}}. \end{cases} \tag{A.5}$$

Similarly, the above relationship comes out with

$$\sqrt{-c-di} = \frac{1}{\sqrt{2}}\left(\sqrt{\sqrt{c^2+d^2}-c} - i\sqrt{\sqrt{c^2+d^2}+c}\right). \tag{A.6}$$

Finally, it can be summarized by the following equations where imaginary parts are thereby eliminated with mathematical transformation and lead to simplified expressions.

$$\begin{aligned} \sqrt{A_2 - A_3 i} &= \frac{1}{\sqrt{2}}\left(\sqrt{\sqrt{A_2^2 + A_3^2} + A_2} - i\sqrt{\sqrt{A_2^2 + A_3^2} - A_2}\right), \\ \sqrt{-a+bi} &= \frac{1}{\sqrt{2}}\left(\sqrt{\sqrt{a^2+b^2}-a} + i\sqrt{\sqrt{a^2+b^2}+a}\right), \end{aligned} \tag{A.7}$$

where

$$\begin{cases} a = c = A_1 + \sqrt{2}\sqrt{\sqrt{A_2^2 + A_3^2} + A_2} > 0, \\ b = d = A_4 + \sqrt{2}\sqrt{\sqrt{A_2^2 + A_3^2} - A_2} > 0. \end{cases} \tag{A.8}$$

Finally, $\lambda 1 + \lambda 2 + \lambda 3 + \lambda 4 = \sqrt{-a+bi} + \sqrt{-c-di} = \sqrt{2}\sqrt{\sqrt{a^2+b^2}-a}$ is further achieved.

Data Availability

Some or all data, models, or codes generated or used during the study are available from the corresponding author by request.

Conflicts of Interest

The authors declare that there are no conflicts of interest.

Authors' Contributions

Yue Xiang conceptualized the data, curated the data, wrote the original draft, and performed code development and validation. Ping Tan conceptualized the data, was responsible for methodology; wrote, reviewed, and edited the draft and was also responsible for supervision. Hui He was responsible for software and validation. Qianmin Chen was responsile for Software.

Acknowledgments

This research was funded by the National Key Research and Development Program of China (Grant no. 2021YFC3100701), the National Natural Science Foundation of China (Grant no. 51978185), the Program for Changjiang Scholars and Innovative Research Team in University (Grant no. IRT13057), the Scientific Research Project of Hunan Education Department, China (Grant no. 22B0858), and the Science and Technology Innovation Project of Hengyang City, China (Grant no. 202250045150).

References

[1] G. W. Housner, L. A. Bergman, T. K. Caughey et al., "Structural control: past, present, and future," *Journal of Engineering Mechanics*, vol. 123, no. 9, pp. 897–971, 1997.

[2] B. F. Spencer Jr. and S. Nagarajaiah, "State of the art of structural control," *Journal of Structural Engineering*, vol. 129, no. 7, pp. 845–856, 2003.

[3] J. P. Den Hartog, *Mechanical Vibrations*, McGraw-Hill, New York, NY, USA, 1956.

[4] H. Frahm, "Device for damping vibrations of bodies," *U.S. Patent No,* vol. 989, pp. 3576–3580, 1911.

[5] J. Ormondroyd and J. P. Den Hartog, "'The theory of the dynamic vibration absorber," *ASME J. Appl. Mech*, vol. 50, no. 7, pp. 9–22, 1928.

[6] G. B. Warburton, "Optimum absorber parameters for various combinations of response and excitation parameters,"

Earthquake Engineering & Structural Dynamics, vol. 10, no. 3, pp. 381–401, 1982.

[7] S. H. Crandall and W. D. Mark, *Random Vibration in Mechanical Systems*, Academic Press, New York, NY, USA, 1963.

[8] T. Asami, T. Wakasono, K. Kameoka, M. Hasegawa, and H. Sekiguchi, "Optimum design of dynamic absorbers for a system subjected to random excitation," *JSME international journal. Ser. 3, Vibration, control engineering, engineering for Industry*, vol. 34, pp. 218–226, 1991.

[9] T. Asami, O. Nishihara, A. M. Baz, and F Kimura, "Closed-form exact solution to H₂ optimization of dynamic vibation absorbers attached to damped linear systems," *TRANSACTIONS OF THE JAPAN SOCIETY OF MECHANICAL ENGINEERS Series C*, vol. 67, no. 655, pp. 597–603, 2001.

[10] S. V. Bakre and R. S. Jangid, "Optimum parameters of Tuned Mass Damper for damped main system," *Structural Control and Health Monitoring*, vol. 14, no. 3, pp. 448–470, 2007.

[11] L. L. Chung, L. Y. Wu, H. H. Huang, C. H. Chang, and K. H. Lien, "Optimal design theories of tuned mass dampers with nonlinear viscous damping," *Earthquake Engineering and Engineering Vibration*, vol. 8, no. 4, pp. 547–560, 2009.

[12] O. F. Tigli, "Optimum vibration absorber (tuned mass damper) design for linear damped systems subjected to random loads," *Journal of Sound and Vibration*, vol. 331, no. 13, pp. 3035–3049, 2012.

[13] T. Asami and O. Nishihara, "H 2 optimization of the three-element type dynamic vibration absorbers," *Journal of Vibration and Acoustics*, vol. 124, no. 4, pp. 583–592, 2002.

[14] H. Chen and P. Tan, "Optimal design of TVMD with linear and nonlinear viscous damping subjected to white-noise excitation," *Structural Control and Health Monitoring*, vol. 28, no. 4, p. 28, 2020.

[15] H Hui, P. Tan, H. Linfei, K. Xu, and X. Yue, "Optimal design of tuned viscous mass damper for acceleration response control of civil structures under seismic excitations," *Engineering Structures*, vol. 252, 2021.

[16] N. O. Myklestad, "The concept of complex damping," *Journal of Applied Mechanics*, vol. 19, no. 3, pp. 284–286, 1952.

[17] R. E. D. Bishop, "The treatment of damping forces in vibration theory," *The Journal of the Royal Aeronautical Society*, vol. 59, no. 539, pp. 738–742, 1955.

[18] T. J. Reid, "Free vibration and hysteretic damping," *The Journal of the Royal Aeronautical Society*, vol. 60, no. 544, p. 283, 1956.

[19] T. K. Caughey and A. Vijayaraghavan, "Free and forced oscillations of a dynamic system with "linear hysteretic damping" (non-linear theory)," *International Journal of Non-linear Mechanics*, vol. 5, no. 3, pp. 533–555, 1970.

[20] G. B. Muravskii, "On frequency independent damping," *Journal of Sound and Vibration*, vol. 274, no. 3-5, pp. 653–668, 2004.

[21] C.-S. Liu, "Reid's passive and semi-active hysteretic oscillators with friction force dependence on displacement," *International Journal of Non-linear Mechanics*, vol. 41, no. 6-7, pp. 775–786, 2006.

[22] Y.-J. Kang, L.-Y. Peng, W. Liu, and Z.-R. Lai, "Steady-state response and damping control effect of reid-TMD," *International Journal of Structural Stability and Dynamics*, vol. 19, no. 10, Article ID 1950122, 2019.

[23] E. Matta and R. Greco, "Modeling and design of tuned mass dampers using sliding variable friction pendulum bearings," *Acta Mechanica*, vol. 231, no. 12, pp. 5021–5046, 2020.

[24] E. Matta, "A novel bidirectional pendulum tuned mass damper using variable homogeneous friction to achieve amplitude-independent control," *Earthquake Engineering & Structural Dynamics*, vol. 48, no. 6, pp. 653–677, 2019.

[25] E. Matta, "Modeling and design of bidirectional pendulum tuned mass dampers using axial or tangential homogeneous friction damping," *Mechanical Systems and Signal Processing*, vol. 116, pp. 392–414, 2019.

[26] S. Nagarajaiah, L. Chen, and M. Wang, "Adaptive stiffness structures with dampers: seismic and wind response reduction using passive negative stiffness and inerter systems," *Journal of Structural Engineering*, vol. 148, no. 11, Article ID 04022179, 2022.

[27] M. Wang, S. Nagarajaiah, and L. Chen, "Adaptive passive negative stiffness and damping for retrofit of existing tall buildings with tuned mass damper: tmd-nsd," *Journal of Structural Engineering*, vol. 148, no. 11, Article ID 0402210, 2022.

[28] Y. Xiang, P. Tan, H. He, J. Shang, and Y. Zhang, "Seismic optimization of variable friction pendulum tuned mass damper with hysteretic damping characteristic," *Soil Dynamics and Earthquake Engineering*, vol. 160, Article ID 107381, 2022.

[29] J. Wang, C. H Lian, and C. C. Lin, "Two-stage optimum design of tuned mass dampers with consideration of stroke," *Structural Control and Health Monitoring*, vol. 16, no. 1, pp. 55–72, 2009.

[30] J. F Wang and C. C Lin, "Development of optimal design theory for series multiple tuned mass dampers considering stroke and multiple structural modes," *Journal of Physics: Conference Series*, vol. 744, Article ID 012231, 2016.

[31] C. C. Lin, J. F Wang, C. H Lien, H. W Chiang, and C. S Lin, "Optimum design and experimental study of multiple tuned mass dampers with limited stroke," *Earthquake Engineering & Structural Dynamics*, vol. 39, 2010.

[32] S. Bakhshinezhad and M. Mohebbi, "Multiple failure function based fragility curves for structures equipped with TMD," *Earthquake Engineering and Engineering Vibration*, vol. 20, no. 2, pp. 471–482, 2021.

[33] E. Matta, "Lifecycle cost optimization of tuned mass dampers for the seismic improvement of inelastic structures," *Earthquake Engineering & Structural Dynamics*, vol. 47, 2017.

[34] D. De Domenico, H. Qiao, Q. Wang, Z. Zhu, and G. Marano, "Optimal design and seismic performance of Multi-Tuned Mass Damper Inerter (MTMDI) applied to adjacent high-rise buildings," *The Structural Design of Tall and Special Buildings*, vol. 29, 2020.

[35] S. Elias, R. Rupakhety, D De Domenico, and S. Olafsson, "Seismic response control of bridges with nonlinear tuned vibration absorbers," *Structures*, vol. 34, 2021.

[36] D. De Domenico, G. Quaranta, G. Ricciardi, and W. Lacarbonara, "Optimum design of tuned mass damper with pinched hysteresis under nonstationary stochastic seismic ground motion," *Mechanical Systems and Signal Processing*, vol. 170, Article ID 108745, 2022.

[37] I. S. Gradshteyn and I. M. Ryzhik, *Table of Integrals, Series, and Products*, Academic, London, UK, 2015.

[38] R. Rana and T. T. Soong, "Parametric study and simplified design of tuned mass dampers," *Engineering Structures*, vol. 20, no. 3, pp. 193–204, 1998.

[39] Applied Technology Council (Atc), "ATC-40 Seismic evaluation and retrofit of concrete buildings," *Appendices. Seismic Safety Commission*, vol. 2, 1996.

[40] N. M. Newmark, E. Rosenblueth, and Y. H. Pao, "Fundamentals of earthquake engineering," *Journal of Applied Mechanics*, vol. 39, no. 2, p. 366, 1972.
[41] Y. Liu, K. Wang, O. Mercan, H. Chen, and P. Tan, "Experimental and numerical studies on the optimal design of tuned mass dampers for vibration control of high-rise structures," *Engineering Structures*, vol. 211, Article ID 110486, 2020.
[42] P. M. Calvi and D. M. Ruggiero, "Numerical modelling of variable friction sliding base isolators," *Bulletin of Earthquake Engineering*, vol. 14, no. 2, pp. 549–568, 2016.
[43] J. Shang, P. Tan, Y. Zhang, J. Han, and P. Mi, "Seismic isolation design of structure using variable friction pendulum bearings," *Soil Dynamics and Earthquake Engineering*, vol. 148, no. 2, Article ID 106855, 2021.
[44] S. Jiying, P. Tan, Y. Zhang, J. Han, and J. Qin, "Experimental and analytical investigation of variable friction pendulum isolator," *Engineering Structures*, vol. 243, Article ID 112575, 2021.
[45] K. Xu, X. Hua, W. Lacarbonara, Z. Huang, and Z. Chen, "Exploration of the nonlinear effect of pendulum tuned mass dampers on vibration control," *Journal of Engineering Mechanics*, vol. 147, no. 8, 2021.
[46] F. Ricciardelli and B. J. Vickery, "Tuned vibration absorbers with dry friction damping," *Earthquake Engineering & Structural Dynamics*, vol. 28, no. 7, pp. 707–723, 1999.
[47] D. De Domenico, G. Ricciardi, S. Infanti, and G. Benzoni, "Frictional heating in double curved surface sliders and its effects on the hysteretic behavior: an experimental study," *Frontiers in Built Environment*, vol. 5, 2019.
[48] E. Gandelli, D De Domenico, P. Dubini, M. Besio, E. Bruschi, and V. Quaglini, "Influence of the breakaway friction on the seismic response of buildings isolated with curved surface sliders: Parametric study and design recommendations," *Structures*, vol. 27, pp. 788–812, 2020.
[49] N. Maia, "Reflections on the hysteretic damping model," *Shock and Vibration*, vol. 16, pp. 529–542, 2009.